THE JOURNAL OF PHYSICAL CHEMISTRY C

Article

pubs.acs.org/JPCC

Plasmonic Nanoantennas for Multispectral Surface-Enhanced Spectroscopies

Heykel Aouani,*[,†] Mohsen Rahmani,[†] Hana Šípová,[‡] Victor Torres,[§] Kateřina Hegnerová,[‡] Miguel Beruete,[§] Jiří Homola,[‡] Minghui Hong,[∥] Miguel Navarro-Cía,[⊥] and Stefan A. Maier[†]

[†]The Blackett Laboratory, Department of Physics, Imperial College London, London SW7 2AZ, United Kingdom

[‡]Institute of Photonics and Electronics, Academy of Sciences of the Czech Republic, Chaberská 57, Prague 18251, Czech Republic

[§]TERALAB (MmW − THz & Plasmonics Laboratory), Universidad Pública de Navarra, Pamplona 31006, Spain

[∥]Department of Electrical and Computer Engineering, National University of Singapore, Singapore 117576, Singapore

[⊥]Optical and Semiconductor Devices Group, Department of Electrical and Electronic Engineering, Imperial College London, London SW7 2BT, United Kingdom

ABSTRACT: Plasmonic nanoantennas provide new routes for efficiently detecting, analyzing, and monitoring single biomolecules via fluorescence, Raman, and infrared absorption spectroscopies. The development of efficient biosensors for multispectral spectroscopy remains nevertheless limited by the narrowband responses of plasmonic devices, as they are generally designed to operate in a specific bandwidth, matching with the absorption, scattering, or emission frequency of target biomolecules under investigation. Therefore, performing biosensing from visible to infrared frequencies systematically requires designing and fabricating multiple plasmonic nanoantenna configurations and prevents the development of nanoscale integrated sensors for multispectral probing of random chemical species. Here, we propose to overcome these limitations by using broadband log-periodic nanoantennas designed to generate significant electromagnetic intensity enhancements from the visible to the mid-IR wavelength regions. We demonstrate simultaneous surface-enhanced fluorescence, Raman, and infrared absorption spectroscopies for biomolecules functionalized on top of single nanoantennas, which opens new opportunities for the development of integrated devices suitable for multispectral biosensing on the same chip.

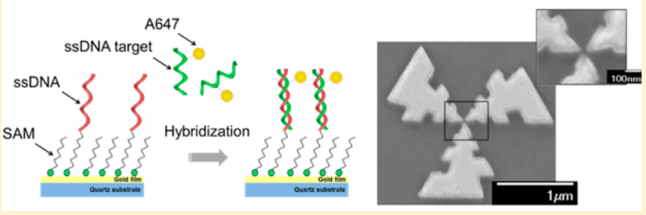

INTRODUCTION

Optical and infrared spectroscopy techniques based on fluorescence, Raman, and infrared absorption contrast are powerful tools for detecting, identifying, or monitoring target molecular species, with major applications in analytical chemistry,[1−3] biology,[4−6] and medicine.[7−9] While fluorescence processes involve a radiative emission between two distinct electronic levels occurring after the absorption of single photons, Raman scattering and infrared absorption processes originate from light interactions with the vibrational levels of a molecule. Although some vibrational modes may be active in both Raman and infrared absorption, these two distinct phenomena arise from different mechanisms with distinct selection rules and lead to complementary information. While spontaneous Raman relies on inelastic scattering occurring after light excitation at a higher frequency and is suitable to probe the symmetric vibrations of nonpolar groups, infrared absorption spectroscopy is based on a direct excitation of the vibrational modes and provides access to the asymmetric vibration characteristics of polar groups.[10] This explains the difference of excitation source natures and frequencies used for Raman and infrared absorption spectroscopy experiments.

Despite significant technological advances, the sensitivity of current luminescence and vibrational spectroscopy setups allows the analysis of molecular species at high concentrations, yet probing samples containing extremely low amounts of molecules remains a challenging task. This is a direct consequence of the detection limits set by the optical diffraction phenomenon, and the weak extinction cross sections of fluorescence, Raman, and infrared absorption mechanisms. Therefore, the complete fingerprinting of target biomolecules at trace, or ultimately the single-molecule level, requires improving the signal-to-noise ratio during spectroscopy experiments via molecular resonance or field enhancement mechanisms.[11]

Electromagnetic field enhancements can be reached on the nanoscale by exploiting the localized surface plasmon modes associated with nanoantennas.[12,13] By efficiently focusing the energy from the far field into subwavelength volumes and locally tailoring the environment surrounding a molecule, plasmonic nanoantennas enable the detection of low concentrations of molecular species via fluorescence,[14−17] Raman,[18−21] and infrared absorption spectroscopies.[22−25] This strategy is nevertheless limited by the narrow band

Received: May 7, 2013
Revised: August 13, 2013
Published: August 13, 2013

   dx.doi.org/10.1021/jp404535x | J. Phys. Chem. C 2013, 117, 18620−18626

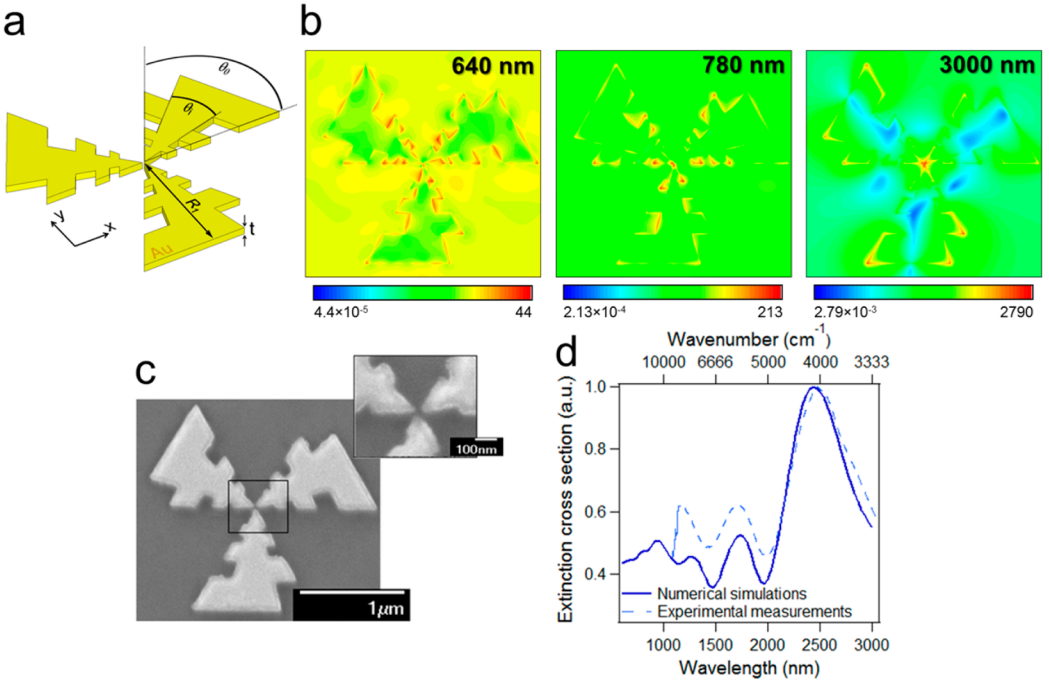

Figure 1. (a) Schematic representation of the three-arm log-periodic gold nanoantenna defined with its geometrical parameters. (b) Intensity enhancement of the electric field with respect to the incident field $\log_{10}(|E(x,y)|^2/|E_0|^2)$ 2 nm above the surface at the specific wavelengths of interest (640, 780, and 3000 nm). (c) SEM image of a fabricated structure. (d) Simulated (solid line) and measured (dashed line) extinction cross section spectrum of the log-periodic nanoantenna.

responses of the simple nanoantenna designs used for enhanced-sensing experiments:[11] rods, spheres, shells, triangles, and dimers or clusters of these nanoparticles. Indeed, because of their dipolar nature, the typical plasmonic resonances associated with these nanoantenna geometries exhibit full widths at half maximum between 50 and 250 nm. Therefore, performing spectroscopy experiments from the visible to the infrared regions systematically requires designing and fabricating multiple plasmonic structure configurations, which is time-consuming and prevents the development of integrated sensors for simultaneously monitoring multiple spectral fingerprint regions or probing random molecular species.

We propose in this paper to overcome these limitations by exploiting the broadband properties of multiresonant nanoantennas recently introduced for nonlinear plasmonics[26−28] and mid-IR spectroscopy applications.[29,30] Our investigations are focused on log-periodic geometries inspired by microwave antenna designs and here transposed into the optical regime, thus providing high local excitation intensity enhancements in a bandwidth of several octaves.[26] We demonstrate that the broadband electromagnetic intensity enhancement generated in the vicinity of these nanoantennas enables surface-enhanced spectroscopy from the visible to the mid-IR using fluorescence, Raman, and infrared absorption processes, which opens new opportunities for the development of integrated devices for multispectral biosensing.

EXPERIMENTAL METHODS

Numerical Simulations. FDTD calculations were performed using FDTD Solutions 8.5.3.[31] The optical constants for the materials were taken from tabulated data: Au,[32] Ti, Cr, and SiO_2.[33] The Drude−Lorentz fitting considered 6, 8, 10, and 6 coefficients to match accurately the experimental dielectric function of Au, Ti, Cr, and SiO_2, respectively. A tolerance of 0.1 was allowed, and passivity of the fitting was enforced. The boundary conditions were set as a perfectly matched layer in every face of the simulation box. The solver-defined total-field scattered-field (TFSF) source was used to reduce computation requirements since it allows defining a plane-wave excitation within a specific volume enclosing only the nanoantenna. In our case, the TFSF box was 2600 nm × 2400 nm × 110 nm. The plane-wave was normal incident to the nanoantenna from the semi-infinite free-space, i.e., propagating along z, and was x-polarized. The details of the incident plane-wave temporal pulse for each simulation are given below. A staircase type mesh with the solver-defined mesh accuracy of 3 was used by default for the whole simulation box. Mesh override regions covering different volumes of the design were used for fine resolution of the geometry. The mesh sizes were set to 4 nm by default for the volume outlined by the TFSF. For the gap region, the volume with dimensions 100 nm × 100 nm × 90 nm was discretized with a cubic grid of 1 nm × 1 nm × 4 nm. A finer mesh size along z of 1 nm was applied for the Ti and Cr layers. The maximum simulation time was set to 500 fs. The time stepping stability factor was set to 0.95, which corresponds to a time step of δt = 0.00183 fs. The residual energy in the simulation box volume was at least −50 dB with respect to its peak value to ensure that the continuous wave information obtained by discrete Fourier transformations was valid. A standard convergence test was done to ensure negligible numerical errors originated from the PML distance, the nonuniform meshing, or the monitor sampling. For the calculation of the extinction cross section, an electromagnetic temporal pulse with wavelength ranging from 500 to 3000 nm (i.e., pulse length ∼3.33 fs) was launched into the box defined by the TFSF source containing the nanoantenna. The extinction cross section was calculated then by the sum of the power flowing outward through a volume enclosing the

dx.doi.org/10.1021/jp404535x | J. Phys. Chem. C 2013, 117, 18620−18626

TFSF source (scattering cross section) and the net power flowing inward through a rectangular cuboid enclosing the nanoantenna but not the TFSF source (absorption cross section). For the intensity enhancement maps of Figure 1, meanwhile, three independent simulations were performed. The central wavelength of the incident electromagnetic temporal pulse of each simulation was 640, 780, and 3000 nm, whereas the pulse length was ~4.23, ~5.15, and ~19.82 fs, respectively. A 2D field profile monitor recorded the field at the *xy* cross section plane 2 nm above the Cr-free-space interface.

Fabrication of the Structures. The log-periodic gold nanoantennas used in this study were fabricated on SiO_2 substrates by electron beam lithography (Elonix 100KV EBL system). Briefly, a thin Ti film (3 nm thick) was deposited on top of the substrate by e-beam evaporation to ensure the adhesion between the evaporated 40 nm Au layer and the SiO_2 substrate. To define the nanoantenna patterns, a 50 nm hydrogen silsesquioxane (HSQ) was used as a negative electroresist. After baking the sample at 200 °C for 2 min, a combined process of e-beam exposure, chemical development, and ion milling was performed to obtain three-arm log-periodic nanoantennas.

Functionalization for Vibrational Spectroscopy Experiments. The Raman and infrared absorption experiments presented in this paper were conducted with streptavidin molecules. Before the functionalization, the substrates were thoroughly rinsed with ethanol and cleaned in UV-ozone cleaner for 5 min. To form the self-assembled monolayer (SAM) of alkanethiols (thickness of 2 nm), the samples were immersed in 200 μM mixed solution of alkanethiols dissolved in ethanol (purity ≥99.9%, Merck, USA). The alkanethiols $HS-(CH_2)_{11}-EG_6-OCH_2-COOH$ (AT−COOH) and $HS-(CH_2)_{11}-EG_4-OH$ (AT−OH) purchased from Prochimia, Poland, were mixed in ratio of 3:7. The immersed substrates were stored at room temperature overnight, rinsed with ethanol and deionized water, and dried with a stream of nitrogen. To activate the carboxylic groups, the chip was incubated for 15 min in aqueous solution of 0.5 M 1-ethyl-3-(3-dimethylaminopropyl)-carbodiimide (EDC) and 0.1 M *N*-hydroxysuccinimide (NHS) (from GE Healthcare, USA). The substrate was then rinsed with deionized water, dried with a stream of nitrogen, and immersed for 2 h in streptavidin solution of 50 μg mL^{-1} concentration in a 10 mM sodium acetate buffer (SA; pH 5 at 25 °C). To wash away the noncovalently bound streptavidin, the sample was washed with a phosphate buffer of high ionic strength (PB_{Na}; 1.4 mM KH_2PO_4, 8 mM Na_2HPO_4, 2.7 mM KCl, 0.75 M NaCl, pH 7.4 at 25 °C), rinsed with water, and dried with a stream of nitrogen. This functionalization procedure yields surface concentrations of streptavidin of around 1.7×10^{12} molecules cm^{-2} on planar surfaces.[34] This value was used for the determination of effective thickness of the streptavidin layer on the nanoantennas.

Functionalization for Fluorescence Spectroscopy Experiments. For fluorescence spectroscopy experiments, the samples were functionalized with DNA probes labeled by fluorescent dyes. For the attachment of the DNA probes, the cleaned substrates were immersed in a 10 μM solution of thiolated DNA probes (SdT_{20}; HS−TEG-5′-dT_{20}-3′) in a phosphate buffer (137 mM NaCl, 1.4 mM KH_2PO_4, 8 mM $Na_2HPO_4 \cdot 12\ H_2O$, 2.7 mM KCl, pH 7.4 at 20 °C) for 30 min. The probes and complementary targets (Alex647−5′-dA_{20}-3′) were purchased from Integrated DNA technologies, USA, in HPLC purity grade. The substrate was rinsed with deionized water and immersed in 100 μM solution of 1-mercapto-6-hexanol (Sigma Aldrich) for 30 min. Hereafter, the substrate was rinsed with deionized water and dried with a stream of nitrogen.

Raman Spectroscopy Measurements. The reference Raman spectrum of streptavidin molecules was measured by using drop-coating deposition Raman spectroscopy (DCDR).[35] The streptavidin was dissolved in SA buffer at 1 mg·mL^{-1} concentration, and 10 μL drops were deposited on BK7 glass plates with a 2 nm layer of TiO_2 and 50 nm of gold. The Raman intensity was measured across the ridge of the drop using a 5 μm step and autofocus after each step. The height profile of the edge of the drop was determined at two distant positions with a Tencor α-step 500 device (scan speed 20 μm/s, stylus force 0.2 mg, and resolution 25A). The width of the drop ridge was 100 μm, and the maximal height of the ridge was set between 5 and 10 μm. For a thickness below 3 μm, the Raman signal was found to be linearly proportional to the layer thickness. The Raman intensity of the δ-CH_2 vibration at 1448 cm^{-1}, corresponding to a monolayer of streptavidin, was calculated by using the linear regression of the measured Raman intensity and the thickness of the drop coating ring.

Infrared Spectroscopy Measurements. The extinction cross section of a log-periodic gold nanoantenna was measured by using a commercial FTIR setup (Bruker Hyperion 2000). The experimental extinction spectra were obtained by integrating the infrared signal from an optical antenna array (2 cm^{-1} resolution, 1000 scans). The absorption of the quartz substrate has been taken into account by subtracting it from the previous spectra, before being normalized by the excitation source profile (determined by using a silver mirror), thus giving access to the extinction spectrum of the nanoantenna.

RESULTS AND DISCUSSION

Modeling of the Log-Periodic Nanoantennas. Finite-difference time-domain (FDTD) calculations[31] were performed for a single log-periodic nanoantenna to design the targeted bandwidth of operation and to interpret the experimental results. The log-periodic nanoantenna used for this study can be seen in Figure 1a. A three-arm design was chosen to obtain polarization independence,[28] due to C_3 rotational symmetry, which also implies that the design allows manipulating circularly polarized waves. The geometry of the nanoantenna is defined with the following parameters matching those measured from high-resolution scanning electron microscopy of the fabricated sample: $R_{m+1}/R_m = (0.49)^{1/2}$ with m = 1, 2, ..., 5 and total length of each arm R_1 = 1000 nm; inner and outer angles, $\Theta_i = 30°$ and $\Theta_0 = 60°$, respectively; metal thickness t = 60 nm; separation between arm vertices $g = 10 \times 3^{1/2}$. For this study, gold (Au) rather than silver was chosen to avoid the quick oxidation of the latter. A 3 nm thick titanium (Ti) ensures the adhesion between the gold film and a SiO_2 substrate. Notice that this nanoantenna provides a systematic approach to enlarge the bandwidth of operation, which facilitates the design procedure.[26] Figure 1b displays the intensity enhancement at the cross-sectional *xy* plane 2 nm above the nanoantenna at three different wavelengths (640, 780, and 3000 nm, corresponding to the spectral positions of the experimentally observed surface-enhanced fluorescence, Raman, and infrared absorption spectroscopy, respectively) when the nanoantenna is illuminated by an *x*-polarized plane wave. This *xy* plane is considered to be representative for the experimental results since the adsorbed biomolecular mono-

dx.doi.org/10.1021/jp404535x | J. Phys. Chem. C 2013, 117, 18620−18626

layer used has an estimated thickness of 2 nm. Note that wavelengths chosen here do not correspond to the first three peaks on the extinction cross section that occur at 2435, 1735, and 1268 nm (see Figure 1d). We point out that for the wavelengths covered by the log-periodic nanoantennas a hot spot is generated at the gap of the structures, which is not the case with multiple length elements. Although the nanoantenna is not operating at the extinction cross-section peaks, where higher intensity enhancements should be expected, the intensity enhancements still reach local values as high as, for instance, 2790 for λ = 3000 nm. At λ = 640 nm and λ = 780 nm, the peak intensity enhancements are significantly lower, but the hot spots are not so localized, and rather the intensity enhancement is more uniform across the whole nanoantenna.

Extinction Cross-Section Measurements. The fabrication quality of the log-periodic nanoantennas was checked by performing high-resolution scanning electron microscopy (Figure 1c). Hereafter, the experimental extinction spectrum of the fabricated structures (defined as 1-transmission) has been determined by Fourier transform infrared spectroscopy (FTIR, Bruker Hyperion 2000) on a square array of 15 × 15 nanoantennas (pitch of 10 μm, ensuring that coupling between neighboring nanoantennas is insignificant) at normal incidence under linear polarization. Details about the FTIR experiments are available in the Experimental section. The measured extinction spectrum of the log-periodic nanoantenna has been superimposed to the simulated extinction cross section of Figure 1d. As can be seen, the measured fundamental resonance is centered at 2504 nm, while the resonances at shorter wavelengths are, respectively, localized at 1721 and 1176 nm, in good agreement with the numerical simulations.

Surface-Enhanced Fluorescence Measurements. The surface-enhanced fluorescence abilities provided by the log-periodic nanoantennas were experimentally investigated by detecting fluorescently labeled DNA. The nanoantennas were functionalized with thiolated DNA probes and mercaptohexanol as a blocking layer. The sample was then incubated with the complementary DNA target sequence labeled with Alexa Fluor 647 molecules (A647, from Integrated DNA Technologies, Inc., quantum yield in solution = 30%, maximum absorption/emission peaks at, respectively, 650/672 nm). A schematic representation of the fluorescently labeled DNA on the functionalized nanoantennas is presented in Figure 2a.

The excitation of A647 molecules was performed by a CW laser diode at 640 nm focused in the sample plane with a 0.5 NA air objective. The same microscope objective was used to collect the fluorescence light emitted from A647 molecules. The incident laser power was set below the fluorescence saturation of A647 molecules, i.e., in a linear excitation regime of the fluorescence emission. Typical fluorescence scanning images of A647 molecules attached to the functionalized nanoantennas are presented in Figure 2b, showing a good reproducibility of the fabrication and functionalization processes. An x-cut in the scanning fluorescence image displayed in Figure 2c can reveal the fluorescence intensity of A647 molecules on top of nanoantennas and on a reference gold film determined under the same excitation power. From these data, the fluorescence enhancement provided by a single log-periodic nanoantenna, defined as the ratio of the fluorescence intensity per A647 molecule with the nanoantenna compared to the reference flat gold film, is estimated as 4.8. As previously reported,[13−15] the fluorescence enhancement generated in the vicinity of a metallic structure originates

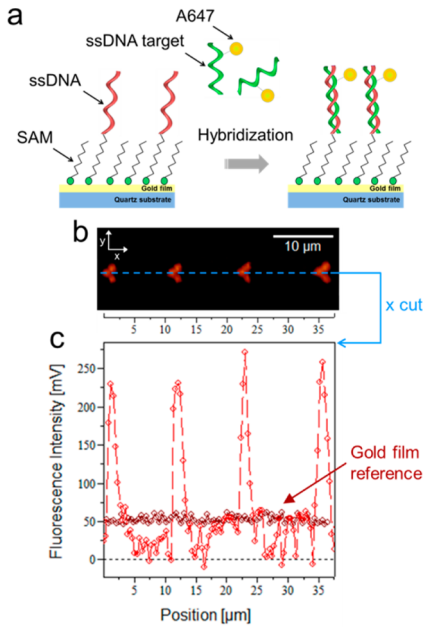

Figure 2. (a) Schematic of detection of the DNA target labeled with Alexa Fluor 647 using DNA probes attached to the gold film. (b) Fluorescence scanning images of four log-periodic nanoantennas and (c) cut according to x-axis revealing the fluorescence intensity for each structure. The fluorescence intensity in the case of functionalization on a flat gold film is also displayed as a reference.

from excitation and emission processes, but determining the respective weight of each contribution is outside the scope of this work. We point out that higher fluorescence enhancements could be reached with the log-periodic gold nanoantenna by positioning a single emitter at the gap or by using fluorescent dyes with lower quantum yield.[15] Further investigations could possibly spatially resolve the fluorescence distribution of molecules attached by using a high numerical aperture objective or high-resolution microscopy.[36]

Surface-Enhanced Raman Measurements. Raman scattering experiments were conducted with streptavidin molecules to access to the surface-enhanced Raman scattering (SERS) gain generated near the log-periodic nanoantennas. The streptavidin molecules were attached to a mixed self-assembled monolayer (SAM) of alkanethiols via a covalent bond created using amine-coupling chemistry, as depicted in Figure 3a.

The Raman spectroscopy experiments described in this section were performed by using a microspectrophotometer (Renishaw InVia) with a resolution of 3 cm^{-1} (integration time of 20 s with five accumulations). The excitation source was provided by a line focus laser diode operating at 785 nm, with an incident power set at 1 mW. A reference Raman spectrum of streptavidin obtained with drop coating deposition Raman spectroscopy (DCDR) is presented in Figure 3b and agrees well with those reported in the literature from both solid and liquid streptavidin.[37,38] The SERS spectra from the log-periodic nanoantennas (two nanoantennas in the laser focus) were determined under the same experimental conditions. A SERS spectrum, obtained as an average from 90 nanoantennas, is presented in Figure 3c. As we can see, the SERS signal from the SAM is much weaker than the signal of streptavidin, which facilitates the SERS analysis of streptavidin molecules. Most of the bands identified in the Raman spectra of streptavidin are

dx.doi.org/10.1021/jp404535x | J. Phys. Chem. C 2013, 117, 18620−18626

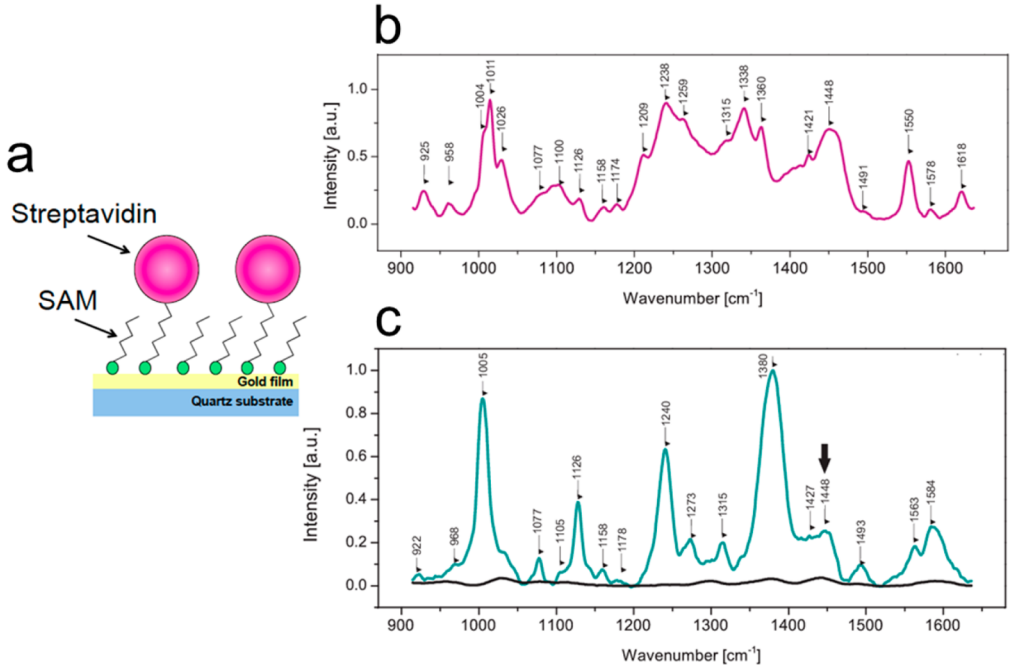

Figure 3. (a) Schematic representation of streptavidin functionalization on top of a gold substrate. (b) Raman spectra of streptavidin obtained with DCDR. (c) SERS spectra of streptavidin immobilized on the SAM of alkanethiols on nanoantennas. Bottom line corresponds to the SERS spectra of the SAM. Black arrow indicates the band used for calculation of the enhancement factor.

present in the SERS spectra from single nanoantennas. However, the relative intensities of bands markedly differ, which can be explained as a result of conformational changes of streptavidin due to its covalent attachment to the surface.[37] The band of δCH_2 at 1448 cm^{-1} was used to calculate the SERS enhancement factor (SERS-EF), as it is supposed to be unaffected by structural changes of the protein. The SERS-EF was determined according to the analytical definition SERS-EF = I_{SERS}/I_{RS}, where I_{SERS} and I_{RS} are, respectively, the SERS and Raman intensities at 1448 cm^{-1} of a streptavidin monolayer under the same experimental conditions. By approximating a streptavidin molecule to a sphere with a radius of 2.5 nm, the effective thickness of the streptavidin layer was calculated to be 1 nm. The Raman intensity I_{RS} of the streptavidin layer with a 1 nm thickness was extrapolated from the DCDR measurements of streptavidin layers with various thicknesses. From these results, the SERS-EF brought by a single nanoantenna was estimated to be 1×10^4, which can be directly correlated to the electromagnetic intensity enhancement in the vicinity of the nanoantenna presented in Figure 1b. Please note that because the streptavidin molecules are positioned on top of the SAM of alkanethiols higher SERS gains could be expected by attaching streptavidin molecules closer to the gold surface.

Surface-Enhanced Infrared Absorption Measurements. The infrared absorption enhancement provided by the log-periodic nanoantennas has been experimentally determined by using the vibrational signatures of adsorbed streptavidin, in the same way as the Raman measurements (Figure 3a). The reference IR absorption spectra of mixed SAMs of alkanethiols and streptavidin molecules adsorbed on a flat gold film presented in Figure 4a were measured under grazing illumination by Fourier transform infrared spectroscopy.

The interactions between the log-periodic nanoantennas and the streptavidin molecules were highlighted by determining the extinction spectrum of the combined system on a square array

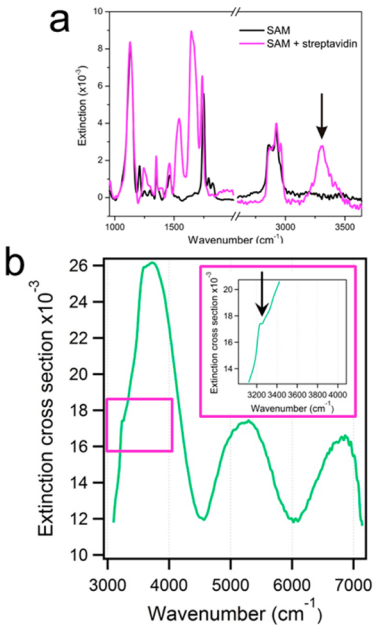

Figure 4. (a) Infrared absorption spectrum of activated mixed SAMs of alkanethiols with and without covalently bound streptavidin molecules measured on flat gold film under grazing illumination. The black arrow indicates the peak corresponding to NH stretching vibrations of streptavidin. (b) Experimental extinction cross section of the three-arm log-periodic gold nanoantenna functionalized with streptavidin. The black arrow corresponds to the Fano interactions between the nanoantennas in the spectrum and the NH stretching vibrations of streptavidin.

of 15 × 15 nanoantennas. Please note that this number could be drastically reduced by using a synchrotron light, as this excitation light source allows single nanoantenna measurements with a good signal-to-noise ratio. As can be seen in Figure 4b,

dx.doi.org/10.1021/jp404535x | J. Phys. Chem. C 2013, 117, 18620−18626

the fundamental resonance of the nanoantenna is affected by the absorption of the streptavidin molecules at 3260 cm^{-1}, leading to a Fano antiresonance profile, as previously reported.[30] Indeed, the dip in the extinction spectrum presented in Figure 4b results from quantum antiphase interactions between the broad resonance of the log-periodic nanoantenna (Figure 1d) and the narrow resonance associated with the characteristic absorption band of proteins at 3260 cm^{-1} (Figure 4b) corresponding to NH stretching vibrations (amide A).[39] The detected size of the infrared absorption signal, defined as the difference between the maximum and minimum extinction at the vibrational mode feature, is estimated to be 0.9% at 3260 cm^{-1}. From these data, we determined the infrared absorption enhancement brought by the nanoantennas, defined as the ratio between the average infrared absorption signal per streptavidin molecule adsorbed on a log-periodic nanoantenna to the average signal per molecule adsorbed on a flat gold film under grazing illumination. Surface-enhanced infrared absorption gains greater than 1.2×10^4 have been determined with six different nanoantenna arrays, resulting from electromagnetic and chemical enhancement mechanisms.[40−43] Please note that vibrational signatures at shorter wavenumbers could be analyzed by increasing the number of teeth of the log-periodic nanoantenna. Moreover, in the same way as the SERS experiments, higher SEIRA gains could be obtained with streptavidin functionalized closer to the surface of nanoantennas. We point out that by accessing the full vibrational spectrum of a molecular complex combining Raman and infrared absorption measurements, the SERS and SEIRA gains provided by our log-periodic nanoantennas could be used for the complete vibrational fingerprinting of target or random biomolecular complexes at low concentrations.

CONCLUSION

In summary, we have investigated in this paper a new class of plasmonic nanoantennas ideally designed for biosensing from the visible to mid-IR regions. The high electromagnetic intensity enhancements generated in the vicinity of our log-periodic nanoantennas enable simultaneous surface-enhanced fluorescence, Raman, and infrared absorption, with relevant enhancement factors. By optimizing several experimental parameters of the functionalization process (selection of fluorescent dyes with lower quantum yield, infrared absorption target molecules closer to the gold surface, etc.), higher fluorescence and vibrational enhancements could be achieved in the selected spectral windows. We believe that these results open new opportunities to develop integrated nanosensors for simultaneously monitoring multiple spectral fingerprint regions or probing random molecular species at low concentrations.

AUTHOR INFORMATION

Corresponding Author

*E-mail: h.aouani@imperial.ac.uk.

Notes

The authors declare no competing financial interest.

ACKNOWLEDGMENTS

H.A. acknowledges stimulating discussions with Yan Francescato. This work was supported by the EPSRC, the U.S. Army International Technology Centre Atlantic (USAITC-A), the Office of Naval Research (ONR and ONR Global), the ESF network PLASMON-BIONANOSENSE, and the Ministry of Education, Youth and Sports of the Czech Republic (contract # LH11102). V.T. acknowledges funding from Universidad Pública de Navarra. M.B. is sponsored by the Spanish Government via RYC-2011-08221. M.N.-C. is supported by the Imperial College Junior Research Fellowship.

REFERENCES

(1) Kim, J.-H.; Heller, D. A.; Jin, H.; Barone, P. W.; Song, C.; Zhang, J.; Trudel, L. J.; Wogan, G. N.; Tannenbaum, S. R.; Strano, M. S. The Rational Design of Nitric Oxide Selectivity in Single-Walled Carbon Nanotube Near-Infrared Fluorescence Sensors for Biological Detection. *Nat. Chem.* **2009**, *1*, 473−481.

(2) McCreery, R. L. *Raman Spectroscopy for Chemical Analysis*; Wiley: New York, 2000.

(3) Ferraro, J. R. *Practical Fourier Transform Infrared Spectroscopy: Industrial and Laboratory Chemical Analysis*; Krishnan, K. K., Eds.; Academic Press: San Diego, CA, 1990.

(4) Walter, N. G.; Huang, C. Y.; Manzo, A. J.; Sobhy, M. A. Do-It-Yourself Guide: How to Use the Modern Single-Molecule Toolkit. *Nat. Methods* **2008**, *5*, 475−489.

(5) Freudiger, C. W.; Min, W.; Saar, B. G.; Lu, S.; Holtom, G. R.; He, C.; Tsai, J. C.; Kang, J. X.; Xie, X. S. Label-Free Biomedical Imaging with High Sensitivity by Stimulated Raman Scattering Microscopy. *Science* **2008**, *322*, 1857−1861.

(6) Holton, S. E.; Walsh, M. J.; Kajdacsy-Balla, A.; Bhargava, R. Label-Free Characterization of Cancer-Activated Fibroblasts Using Infrared Spectroscopic Imaging. *Biophys. J.* **2011**, *101*, 1513−1521.

(7) Urano, Y.; Asanuma, D.; Hama, Y.; Koyama, Y.; Barrett, T.; Kamiya, M.; Nagano, T.; Watanabe, T.; Hasegawa, A.; Choyke, P. L.; Kobayashi, H. Selective Molecular Imaging of Viable Cancer Cells with pH-Activatable Fluorescence Probes. *Nat. Med.* **2009**, *15*, 104−109.

(8) Haka, A. S.; Volynskaya, Z.; Gardecki, J. A.; Nazemi, J.; Lyons, J.; Hicks, D.; Fitzmaurice, M.; Dasari, R. R.; Crowe, J. P.; Feld, M. S. In Vivo Margin Assessment During Partial Mastectomy Breast Surgery Using Raman Spectroscopy. *Cancer Res.* **2006**, *66*, 3317−3322.

(9) Kidder, L. H.; Kalasinsky, V. F.; Luke, J. L.; Levin, I. W.; Lewis, E. N. Visualization of Silicone Gel in Human Breast Tissue Using New Infrared Imaging Spectroscopy. *Nat. Med.* **1997**, *3*, 235−237.

(10) Larkin, P. J. *IR and Raman Spectroscopy*; Jones and Bartlett Publishers, Inc: Burlington, MA, 2005.

(11) Bharadwaj, P.; Deutsch, B.; Novotny, L. Optical Antennas. *Adv. Opt. Photonics* **2009**, *1*, 438−483.

(12) Novotny, L.; van-Hulst, N. F. Antennas for Light. *Nat. Photonics* **2011**, *5*, 83−90.

(13) Giannini, V.; Fernandez-Dominguez, A. I.; Heck, S. C.; Maier, S. A. Plasmonic Nanoantennas: Fundamentals and Their Use in Controlling the Radiative Properties of Nanoemitters. *Chem. Rev.* **2011**, *111*, 3888−3912.

(14) Anger, P.; Bharadwaj, P.; Novotny, L. Enhancement and Quenching of Single-Molecule Fluorescence. *Phys. Rev. Lett.* **2006**, *96*, 113002.

(15) Giannini, V.; Fernández-Domínguez, A. I.; Sonnefraud, Y.; Roschuk, T.; Fernández-García, R.; Maier, S. A. Controlling Light Localization and Light−Matter Interactions with Nanoplasmonics. *Small* **2010**, *6*, 2498−2507.

(16) Kinkhabwala, A.; Yu, Z. F.; Fan, S. H.; Avlasevich, Y.; Mullen, K.; Moerner, W. E. Large Single-Molecule Fluorescence Enhancements Produced by a Bowtie Nanoantenna. *Nat. Photonics* **2009**, *3*, 654−657.

(17) Aouani, H.; Mahboub, O.; Bonod, N.; Devaux, E.; Popov, E.; Rigneault, H.; Ebbesen, T. W.; Wenger, J. Bright Unidirectional Fluorescence Emission of Molecules in a Nanoaperture with Plasmonic Corrugations. *Nano Lett.* **2011**, *11*, 637−644.

(18) Yan, B.; Thubagere, A.; Premasiri, W. R.; Ziegler, L. D.; Dal Negro, L.; Reinhard, B. M. Engineered SERS Substrates with Multiscale Signal Enhancement: Nanoparticle Cluster Arrays. *ACS Nano* **2009**, *3*, 1190−1202.

(19) Brolo, A. G.; Arctander, E.; Gordon, R.; Leathem, B.; Kavanagh, K. L. Nanohole-Enhanced Raman Scattering. *Nano Lett.* **2004**, *4*, 2015−2018.
(20) Ward, D. R.; Grady, N. K.; Levin, C. S.; Halas, N. J.; Wu, Y.; Nordlander, P.; Natelson, D. Electromigrated Nanoscale Gaps for Surface-Enhanced Raman Spectroscopy. *Nano Lett.* **2007**, *7*, 1396−1400.
(21) Li, K.; Stockman, M. I.; Bergman, D. J. Self-Similar Chain of Metal Nanospheres as an Efficient Nanolens. *Phys. Rev. Lett.* **2003**, *91*, 227402.
(22) Neubrech, F.; Pucci, A.; Cornelius, T. W.; Karim, S.; Garcia-Etxarri, A.; Aizpurua, J. Resonant Plasmonic and Vibrational Coupling in a Tailored Nanoantenna for Infrared Detection. *Phys. Rev. Lett.* **2008**, *101*, 157403.
(23) Pryce, I. M.; Aydin, K.; Kelaita, Y. A.; Briggs, R. M.; Atwater, H. A. Highly Strained Compliant Optical Metamaterials with Large Frequency Tunability. *Nano Lett.* **2010**, *10*, 4222−4227.
(24) Kundu, J.; Le, F.; Nordlander, P.; Halas, N. J. Surface Enhanced Infrared Absorption (SEIRA) Spectroscopy on Nanoshell Aggregate Substrates. *Chem. Phys. Lett.* **2008**, *452*, 115−119.
(25) Brown, L. V.; Zhao, K.; King, N.; Sobhani, H.; Nordlander, P.; Halas, N. J. Surface-Enhanced Infrared Absorption Using Individual Cross Antennas Tailored to Chemical Moieties. *J. Am. Chem. Soc.* **2013**, *135*, 3688−3695.
(26) Navarro-Cia, M.; Maier, S. A. Broad-Band Near-Infrared Plasmonic Nanoantennas for Higher Harmonic Generation. *ACS Nano* **2012**, *6*, 3537−3544.
(27) Harutyunyan, H.; Volpe, G.; Quidant, R.; Novotny, L. Enhancing the Nonlinear Optical Response Using Multifrequency Resonant Gold-Nanowire Antennas. *Phys. Rev. Lett.* **2012**, *108*, 217403.
(28) Aouani, H.; Navarro-Cia, M.; Rahmani, M.; Sidiropoulos, T. P. H.; Hong, M.; Oulton, R. F.; Maier, S. A. Multiresonant Broadband Optical Antennas As Efficient Tunable Nanosources of Second Harmonic Light. *Nano Lett.* **2012**, *12*, 4997−5002.
(29) Chen, K.; Adato, R.; Altug, H. Dual-Band Perfect Absorber for Multispectral Plasmon-Enhanced Infrared Spectroscopy. *ACS Nano* **2012**, *6*, 7998−8006.
(30) Aouani, H.; Šípová, H.; Rahmani, M.; Navarro-Cia, M.; Hegnerová, K.; Homola, J.; Hong, M.; Maier, S. A. Ultrasensitive Broadband Probing of Molecular Vibrational Modes with Multifrequency Optical Antennas. *ACS Nano* **2013**, *7*, 669−675.
(31) http://www.lumerical.com.
(32) Johnson, P. B.; Christy, R. W. Optical Constants of the Noble Metals. *Phys. Rev. B* **1972**, *6*, 4370−4379.
(33) Palik, E. D. *Handbook of Optical Constants of Solids*; Academic Press: San Diego, CA, 1998.
(34) Springer, T.; Sipova, H.; Vaisocherova, H.; Stepanek, J.; Homola, J. Shielding Effect of Monovalent and Divalent Cations on Solid-Phase DNA Hybridization: Surface Plasmon Resonance Biosensor Study. *Nucleic Acids Res.* **2010**, *38*, 7343−7351.
(35) Kopecky, V.; Baumruk, V. Structure of the Ring in Drop Coating Deposited Proteins and its Implication for Raman Spectroscopy of Biomolecules. *Vib. Spectrosc.* **2006**, *42*, 184−187.
(36) Cox, S.; Rosten, E.; Monypenny, J.; Jovanovic-Talisman, T.; Burnette, D. T.; Lippincott-Schwartz, J.; Jones, G. E.; Heintzmann, R. Bayesian Localization Microscopy Reveals Nanoscale Podosome Dynamics. *Nat. Methods* **2012**, *9*, 195−200.
(37) Galarreta, B. C.; Norton, P. R.; Lagugne-Labarthet, F. SERS Detection of Streptavidin/Biotin Monolayer Assemblies. *Langmuir* **2011**, *27*, 1494−1498.
(38) Torreggiani, A.; Fini, G. The Binding of Biotin Analogues by Streptavidin: a Raman Spectroscopic Study. *Biospectroscopy* **1998**, *4*, 197−208.
(39) Barth, A. Infrared Spectroscopy of Proteins. *Biochim. Biophys. Acta, Bioenergetics* **2007**, *1767*, 1073−1101.
(40) Osawa, M.; Ikeda, M. Surface-Enhanced Infrared Absorption of P-Nitrobenzoic Acid Deposited on Silver Island Films: Contributions of Electromagnetic and Chemical Mechanisms. *J. Phys. Chem.* **1991**, *95*, 9914−9919.
(41) Merklin, G. T.; Griffith, P. R. Influence of Chemical Interactions on the Surface-Enhanced Infrared Absorption Spectrometry of Nitrophenols on Copper and Silver Surfaces. *Langmuir* **1997**, *13*, 6159−6163.
(42) Krauth, O.; Fahsold, G.; Pucci, A. Asymmetric Line Shapes and Surface Enhanced Infrared Absorption of CO Adsorbed on Thin Iron Films on MgO(001). *J. Chem. Phys.* **1999**, *110*, 3113−3117.
(43) Alonso-González, P.; Albella, P.; Schnell, M.; Chen, J.; Huth, F.; Garca-Etxarri, A.; Casanova, F.; Golmar, F.; Arzubiaga, L.; Hueso, L. E.; et al. Resolving the Electromagnetic Mechanism of Surface-Enhanced Light Scattering at Single Hot Spots. *Nat. Commun.* **2012**, *3*, 684.